ACS APPLIED MATERIALS & INTERFACES

Research Article

www.acsami.org

Bias-Enhanced Nucleation and Growth Processes for Ultrananocrystalline Diamond Films in Ar/CH_4 Plasma and Their Enhanced Plasma Illumination Properties

Adhimoorthy Saravanan,[†] Bohr-Ran Huang,[†] Kamatchi Jothiramalingam Sankaran,[‡] Srinivasu Kunuku,[§] Chung-Li Dong,[⊥] Keh-Chyang Leou,[§] Nyan-Hwa Tai,[‡] and I-Nan Lin[#,*]

[†]Graduate Institute of Electro-Optical Engineering and Department of Electronic Engineering, National Taiwan University of Science and Technology, Taipei 106, Taiwan R.O.C.

[‡]Department of Materials Science and Engineering and [§]Department of Engineering and System Science, National Tsing Hua University, Hsinchu 300, Taiwan R.O.C.

[⊥]Scientific Research Division, National Synchrotron Radiation Research Center, Hsinchu 300, Taiwan R. O. C.

[#]Department of Physics, Tamkang University, Tamsui 251, Taiwan R.O.C.

Supporting Information

ABSTRACT: Microstructural evolution of ultrananocrystalline diamond (UNCD) films in the bias-enhanced nucleation and growth (BEN-BEG) process in CH_4/Ar plasma is systematically investigated. The BEN-BEG UNCD films possess higher growth rate and better electron field emission (EFE) and plasma illumination (PI) properties than those of the films grown without bias. Transmission electron microscopy investigation reveals that the diamond grains are formed at the beginning of growth for films grown by applying the bias voltage, whereas the amorphous carbon forms first and needs more than 30 min for the formation of diamond grains for the films grown without bias. Moreover, the application of bias voltage stimulates the formation of the nanographite phases in the grain boundaries of the UNCD films such that the electrons can be transported easily along the graphite phases to the emitting surface, resulting in superior EFE properties and thus leading to better PI behavior. Interestingly, the 10 min grown UNCD films under bias offer the lowest turn-on field of 4.2 V/μm with the highest EFE current density of 2.6 mA/cm^2 at an applied field of 7.85 V/μm. Such superior EFE properties attained for 10 min bias grown UNCD films leads to better plasma illumination (PI) properties, i.e., they show the smallest threshold field of 3300 V/cm with largest PI current density of 2.10 mA/cm^2 at an applied field of 5750 V/cm.

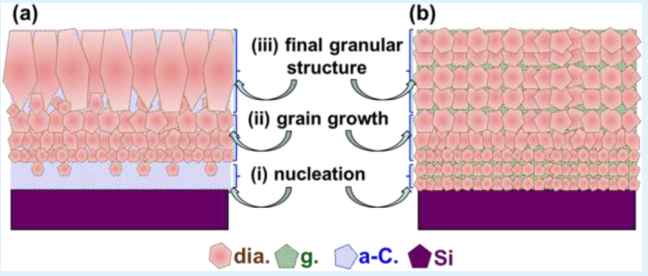

KEYWORDS: *ultrananocrystalline diamond films, bias-enhanced nucleation and growth, nanographitic phases, amorphous carbon, electron field emission, plasma illumination*

INTRODUCTION

The admirable properties of diamond namely tremendous hardness, low friction coefficient, chemical inertness, high electrical resistivity, and its semiconducting properties makes it an attractive material for several applications.[1−3] Diamond has the most strongly bonded crystal structure, such that the field emission devices from diamond material possibly will maneuver with supreme reliability and consistency. Diamond holds a wide bandgap energy (E_g, 5.5 eV), which enables outstanding physical and chemical properties, thereby making it as one of the strongly competing cold cathode materials for the field emission applications and facilitates possible application in flat panel displays and microelectronic devices.[4] The negative electron affinity (NEA) characteristic of diamond films observed for renovate surface is thought to be of great potential for applications as electron field emitters.[5−7] In addition, the diamond plays a significant role in the application of plasma illumination (PI) devices, as it usually exhibits a large secondary electron emission coefficient (γ-coefficient). The Paschen-curve-based γ-coefficient measurement indicates that diamond films synthesized using chemical vapor deposition own a higher γ-coefficient than that of single crystal MgO.[8] The research group of Chakrabarti reported that the high γ-coefficient is associated with better electron field emission (EFE) properties.[9] As a result, the high EFE diamond material is being explored for the development of a high γ-coefficient diamond material with enhanced PI characteristics.

The diamond films grown in CH_4/H_2 plasma were called microcrystalline diamond (MCD) films which contains large sized diamond grains. It also possesses a large electronic

Received: April 12, 2014
Accepted: June 19, 2014
Published: June 19, 2014

bandgap which holds back the EFE behavior of the material essential for field emission due to electrons deficiency.[10−12] Therefore, to improve the EFE properties, the CH_4/Ar plasma has been used to prepare ultrananocrystalline diamond (UNCD) films with nanosized grains and grain boundaries of significant thickness, containing sp^2-bonds and acquiring excellent conductivity.[13,14] The transport of electrons through the UNCD films is noticeably superior to the MCD films and possesses better EFE properties than that of the MCD films.[15,16] The nucleation of diamond grains for the growth of UNCD films is successfully achieved with the following methods: mechanical scratching of the substrate surface using diamond powder, ultrasonic agitation of the substrate surface in a solution containing nanodiamond powder, deposition of a carbide interlayer for assisting diamond nucleation, and bias-enhanced nucleation and growth (BEN-BEG) process. Among the effective diamond seeding and nucleation techniques, the BEN-BEG method is more efficient in reducing the size of the diamond grains.[17,18] Teng et al.[19] reported the enhanced EFE behavior of BEG grown nanocrystalline diamond films using CH_4/H_2 plasma. However, to the best of our knowledge, BEN-BEG process has been demonstrated to be effective only for the CH_4/H_2 plasma and the feasibility of bias enhanced growth of UNCD films using CH_4/Ar plasma has not been reported yet.

In this paper, we have successfully grown UNCD films in CH_4/Ar plasma using negative biased voltage, which resulted in improved PI and EFE properties. The bias voltage was set at −200 V during the UNCD film deposition in each different growth time. This negative bias voltage enhanced the growth of UNCD film even in the minimum growth time of 10 min and the diamond grains were formed effectively. The UNCD growth of 10 min contains smaller grain size with graphitic grain boundaries which offers better electron conduction in the film to facilitate the enhancement in PI properties. In contrast, we observe that the films grown without bias voltage formed only a-C phases at the beginning of film's growth, resulting in inferior EFE and PI properties.

EXPERIMENTAL METHODS

The UNCD films were grown on *n*-type silicon substrates by MPECVD system. Prior to the deposition of UNCD films, the silicon substrates were preseeded by ultrasonication in methanol solution, containing nanosized diamond powders (∼5 nm) and Ti powders (∼32.5 nm) for 45 min.[20] The substrates were ultrasonicated again in methanol for 1 min to eradicate the possibly adhered nanoparticles. The UNCD films were grown in CH_4 (2%)/Ar (98%) plasma (100 sccm), which was excited by a 1200 W microwave power with a 150 Torr total pressure. A negative bias voltage (−200 V) was applied to the Si substrate when the pressure reached 150 Torr in the growth period (10−60 min) of the UNCD films. The corresponding films were designated as $UNCD_{Bn}$, where n is the growth time. In addition, the UNCD films without bias at different growth period (10−60 min) were grown to facilitate the comparison and the corresponding films were designated as $UNCD_{Nn}$, where n is the growth time. The films were characterized using field emission scanning electron microscopy (FESEM; Jeol JSM-6500F), Raman spectroscopy (λ: 632.8 nm, Lab Raman HR800, Jobin Yvon) and near edge X-ray absorption spectroscopy (NEXAFS). The detailed microstructure and bonding structure of the samples were examined using transmission electron microscopy (TEM; Jeol 2100F) and electron energy loss spectroscopy (EELS, Gatan Enfina), respectively.

To investigate the plasma illumination (PI) characteristics of a microplasma device, which used UNCD films as cathode, an indium tin oxide (ITO)-coated glass was used as anode and the cathode-to-anode separation was fixed by a polytetrafluoroethylene (PTFE) spacer (1.0 mm in thickness). A circular hole about 3.0 mm in diameter was cut out from the (PTFE) spacer to form a microcavity. The plasma was triggered using a pulsed direct current voltage in a bipolar pulse mode (20 ms square pulse, 6 kHz repetition rate). Prior to measurements, all samples were heated at 200 °C for 1 h to remove moisture from the surface of the films. The chamber was evacuated to reach a base pressure of 0.1 mTorr and then purged with Ar for 10 min up to 10 Torr. The Ar gas was channeled into the chamber at a flow rate of 10 sccm throughout the measurements. The plasma current versus applied voltage characteristics was measured using an electrometer (Keithley 237).

In contrast, the EFE properties of the diamond films were measured with a tunable parallel plate setup, in which the tungsten rod about 3 mm in diameter was used as anode and the diamond films was used as cathode. The cathode-to-anode distance was controlled using a micrometer. The current−voltage (I−V) characteristics were measured using an electrometer (Keithley 2410) under pressure below 1×10^{-6} Torr. The EFE parameters were extracted from the obtained I−V curves by using the Fowler-Nordheim (F−N) equation,[21] where J_e is the EFE current density and E is the applied field calculated from the I and V, respectively,

$$J_e = \left(\frac{A\beta^2E^2}{\varphi}\right)\exp\left(-\frac{B\varnothing^{3/2}}{\beta E}\right) \quad (2)$$

where $A = 1.54 \times 10^{-6}$ A eV/V^2 and $B = 6.83 \times 10^9$ eV$^{-3/2}$ V/m, β is the field-enhancement factor, E is the applied field, and φ is the work function of the emitting materials. The turn-on field (E_0) was designated as the point of interception of the straight lines extrapolated from the low and high-field segments of the F−N plots, namely, ln (J_e/E^2) versus $1/E$ plots.

RESULTS AND DISCUSSION

A. Plasma Illumination Behavior of the Microplasma Devices. The PI characteristics of the plasma devices using UNCD films grown with and without applied bias at various growth times as cathode are illustrated by the variation of the plasma current density (J_{PI}) versus applied field (E), which is plotted in Figure 1a, b, respectively. Typical photographs showing the PI characteristics of the microplasma devices using these diamond films as cathode are illustrated in the insets of Figure 1. For both series of UNCD films, as the growth time increases, the threshold field for inducing the plasma (E_{th} value) increases, while the plasma current density (J_{PI} value) decreases. The E_{th} values are smaller for the devices using $UNCD_{Bn}$ films as the cathode compared with those using $UNCD_{Nn}$ films as the cathode. The E_{th} is lowest for the microplasma devices using $UNCD_{B10}$-films as the cathode materials. For UNCD films grown using bias, the J_{PI} at 4000 V/cm decreases monotonously from $(J_{PI})_{B10}$ = 0.66 mA/cm^2 to $(J_{PI})_{B60}$ = 0.49 mA/cm^2 (Figure 1a). Restated, the lowest E_{th} value of 3300 V/cm and the largest J_{PI} of 0.66 mA/cm^2 at 4000 V/cm applied field are observed for the $UNCD_{B10}$ films (curve I, Figure 1a). Notably, the J_{PI} value was evaluated at 4000 V/cm, because this is the value used for practical application. The same trend is observed for the films grown without bias, i.e., the $(J_{PI})_{N10}$ = 0.57 mA/cm^2 and (J_{PI}) = 0.34 mA/cm^2 at 4000 V/cm (Figure 1b). The PI parameters are summarized in Table 1, where the J_{PI} values at 5750 V/cm are included to facilitate the comparison.

The secondary electron emission coefficient (γ-coefficient) of these UNCD films were evaluated by "Paschen curves" technique (see the Supporting Information, Figure S2). The γ-coefficients values are included in Table 1, which indicates that the $UNCD_{B10}$ films show slightly higher γ value (0.1315) than that of the other UNCD films (0.1300−0.1255). However,

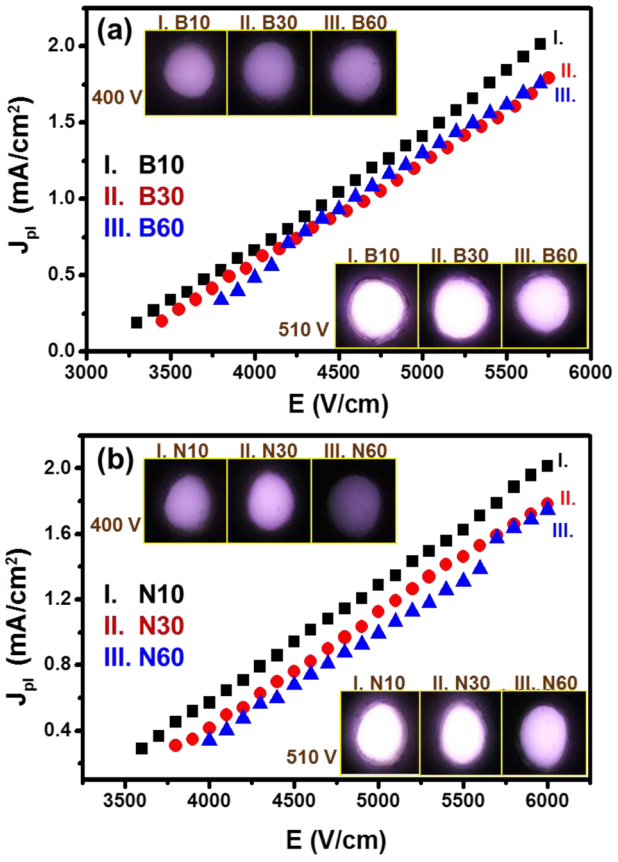

Figure 1. Plasma illumination properties, the plasma current density against applied field, J_{PI}–E curves, of UNCD films deposited for different growth times in (a) bias (−200 V) and (b) no bias. The insets show the typical plasma illumination images of the microplasma devices excited at the designated voltage.

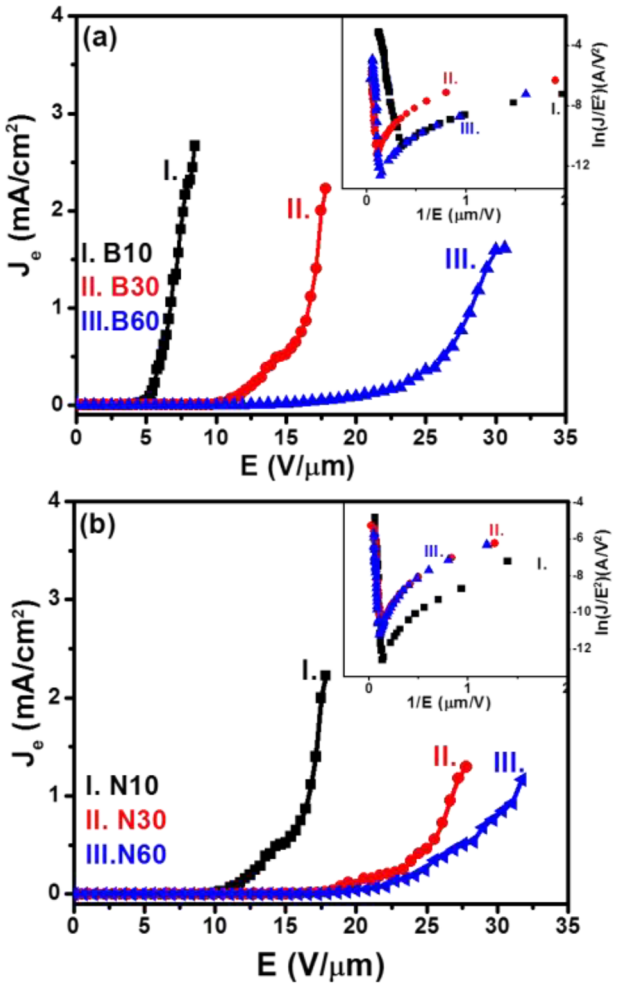

Figure 2. EFE properties of UNCD films deposited for different growth times in (a) bias (−200 V) and (b) no bias. The insets show the corresponding Fowler–Nordheim plots.

the difference in γ value is not large enough to account for the big change in J_{PI} against the cathode materials. The other possible source of electrons for igniting the plasma is the field emitted electrons from the cathode materials. Therefore, the EFE properties of the diamond cathode materials were evaluated. Panels a and b in Figure 2 show the EFE properties of the $UNCD_{Bn}$ and $UNCD_{Nn}$ films deposited in CH_4/Ar plasma using bias and no bias, respectively, which are plotted as the EFE current density versus applied field (J_e–E) with the corresponding F–N plotted shown in the insets. The EFE parameters, the turn-on field (E_0) and the EFE current density at the designated applied field (J_e), are extracted from these plots and are listed in Table 2. For both series of films, E_0 increases with growth time. The $UNCD_{Bn}$ films grown using bias show better EFE behavior, i.e., the lower E_0 and the higher J_e, than the $UNCD_{Nn}$ films grown using no bias. Particularly, the $UNCD_{B10}$ films possess the lowest E_0 value of 4.2 V/μm and the highest J_e value of 2.6 mA/cm^2 at the applied field of 7.85 V/μm. These observations indicate that the PI behavior of the microplasma devices performs better when the cathode materials possess superior EFE properties.

It should be mentioned that the $(E_{th})_{PI}$ required to trigger the Ar plasma for the microplasma devices using diamond as cathodes is perceptibly smaller than the $(E_0)_{EFE}$ for inducing the EFE process. Although the $UNCD_{B10}$ films possess much lower $(E_0)_{EFE}$ (4.2 V/μm) for the EFE process as compared to that of the other UNCD films ($(E_0)_{EFE}$ = 9.8–18.4 V/μm, cf. Table 2). The $(E_{th})_{PI}$ for triggering the PI process does not show much difference when the cathode material is changed from the $UNCD_{B10}$ to $UNCD_{B60}$ (or $UNCD_{Nn}$) films (E_{th} = 3300–3900 V/cm). Such a phenomenon is due to the

Table 1. Plasma Illumination Properties of UNCD Films Deposited for Different Growth Times with Bias ($UNCD_{Bn}$ series) and without Bias ($UNCD_{Nn}$ series) in CH_4/Ar Plasma

	$UNCD_{Bn}$ series				$UNCD_{Nn}$ series			
growth time	E_{th} (V/cm)	J_{PI} (mA/cm^2) @ 4000 (V/cm)	J_{PI} (mA/cm^2) @ 5750 (V/cm)	γ-coefficient	E_{th} (V/cm)	J_{PI} (mA/cm^2) @ 4000 (V/cm)	J_{PI} (mA/cm^2) @ 5750 (V/cm)	γ-coefficient
10	3300	0.66	2.01	0.1315	3600	0.57	1.88	0.1286
30	3500	0.54	1.79	0.1300	3600	0.41	1.61	0.1270
60	3900	0.49	1.76	0.1270	3800	0.34	1.59	0.1255

dx.doi.org/10.1021/am502231d | ACS Appl. Mater. Interfaces 2014, 6, 10566–10575

Table 2. Electron Field-Emission Properties of UNCD Films Deposited at Different Growth Times with Bias ($UNCD_{Bn}$ series) and without Bias ($UNCD_{Nn}$ series) in CH_4/Ar Plasma

	$UNCD_{Bn}$ series			$UNCD_{Nn}$ series		
growth time	E_0 (V/μm)	J_e (mA/cm^2) @ (V/μm)	thickness (nm)	E_0 (V/μm)	J_e (mA/cm^2) @ (V/μm)	thickness (nm)
10	4.2	2.6 @ 7.85	380	10.8	2.2 @ 17.5	260
30	9.8	2.2 @ 18.0	470	16.6	1.2 @ 27.5	340
60	14.6	1.6 @ 30.5	650	18.4	1.1 @ 32.0	515

E_0: the turn-on field for EFE process that was designated as the point of interception of the straight lines extrapolated from the low and high-field segments of the F−N plots, namely, ln (J_e/E^2) versus $1/E$ plots. J_e: the EFE current density evaluated at an applied field designated in parentheses.

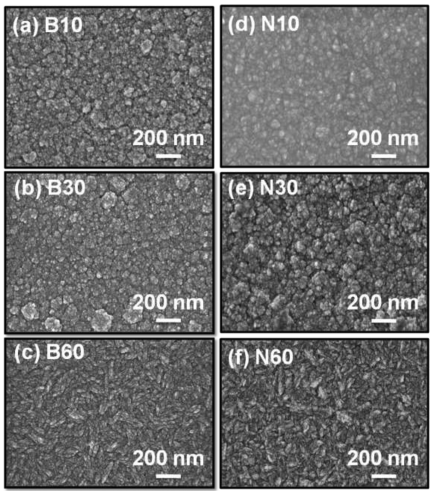

Figure 3. FESEM micrographs of UNCD films, which were grown using BEG under −200 V ((a) B10, (b) B30, and (c) B60) and no bias voltage ((d) N10, (e) N30, and (f) N60) in different growth times, where the number indicates the growth time.

difference in the mechanism for igniting plasma in an Ar environment and that for turning on the EFE process in a high vacuum environment (1×10^{-6} Torr). In a microplasma device, the plasma can be triggered when the electrons emitted from the cathode (secondary electrons) gain sufficient kinetic energy to ionize the gas molecules (e.g., 15.7 eV for Ar species). The ionization cross-section for Ar species increases with kinetic energy of the electrons and reaches a maximum value at around 100 eV.[22] Before the onset of plasma, the electric field imposed on the cathode materials is far below the E_0 needed for inducing the EFE process. Only the ion-bombardment induced secondary electrons contribute to trigger the ionization of Ar gas molecules for inducing the PI process. Therefore, it seems that the small EFE $(E_0)_{EFE}$ for the $UNCD_{B10}$ films is not helpful in lowering the threshold field for igniting the plasma. However, when the plasma is ignited, a plasma sheath is formed in the vicinity of cathode, where the electric field will be markedly increased. For typical plasma with a sheath around 10 μm in thickness, the electric field experienced by the cathode will increase to around 3300 V/cm corresponding to an applied voltage of 330 V. Such a field is far larger than that necessary for turning on the EFE process for most of the diamond films. A large number of electrons will be field emitted from the diamond cathode materials that increases the cascading ionization for the Ar gas molecules and markedly increases the J_{PI}. Therefore, a larger J_{PI} is observed for the microplasma devices when the $UNCD_{B10}$ films were used as cathodes, i.e., (J_{PI}) = 0.66 mA/cm^2 at 4000 V/cm, as they emit more EFE current density.

B. Structural Analyses for the UNCD Cathode Materials. Figure 3 shows the FESEM micrographs of the UNCD films grown with and without applied bias at various growth times. The morphology of the films change due to the application of bias voltage and the change in growth time. The morphology of the $UNCD_{B10}$ shows equi-axed structured grains in the films (Figure 3a). Although the $UNCD_{B30}$ show a similar morphology as $UNCD_{B10}$ (Figure 3b), the $UNCD_{B60}$ shows the elongated grains (Figure 3c), indicating the occurrence of lateral growth of grains for 60 min grown time. On the other hand, the FESEM micrograph shows only blurred image for the films grown without bias at 10 min ($UNCD_{N10}$), implying that the granular structure of films has not yet completely formed (Figure 3d). It takes 30 min growth time to develop a granular structure similar to that of typical UNCD films (Figure 3e). In addition, $UNCD_{N60}$ films (Figure 3f) show the elongated grains as like $UNCD_{B60}$ films but the size of the grains is slightly larger. Notably, the grains in BEG grown $UNCD_{B30}$ (or $UNCD_{B60}$) films appear more densely packed as compared with the $UNCD_{N30}$ (or $UNCD_{N60}$) films grown without bias voltage. Notably, the difference in morphology of the films mainly induced by the interaction of species in the plasma with the priori deposited films due to the application of bias voltage, s the optical emission spectroscopy (OES) shown as Figure S2 in the Supporting Information revealed that the constituents in the plasma neither change due to the application of bias voltage nor with the growth time. The thicknesses of the UNCD films were estimated from the cross-section FESEM micrographs of the films (Figures not shown) and the results are listed in Table 2 (see the Supporting Information, inset in Figure S2). The thickness is ∼380 nm for $UNCD_{B10}$ films and was nearly doubled for $UNCD_{B60}$ films. The thickness decreases rapidly for UNCD films grown without bias. The $UNCD_{N10}$ films show the thickness of ∼260 nm, whereas the $UNCD_{N60}$ films show the thickness of ∼515 nm (curve II, Figure S2 in the Supporting Information). From these observations, we can conclude that by applying bias, the growth rate of the films was increased.

Raman spectroscopy is an important technique to explore the bonding character of different carbon phases present in UNCD films. Panels a and b in Figure 4 depict the visible-Raman spectra of UNCD samples deposited in CH_4/Ar plasma with and without bias at different growth time. Three prominent broad peaks are observed in the spectra for both sets of films. The Raman spectra were deconvoluted using Lorentz functions after normalization of the resonance peaks that were illustrated for spectra I in Figure 4a, b. There is ν_1 (∼1140 cm^{-1}), which originates because of the vibration of *trans*-polyacetylene (*t*-PA) segments present at the grain boundaries.[23,24] Another peak, called breathing modes of the D-band (∼1330 cm^{-1}), is attributed to the disorder-activated aromatic modes of A_{1g} symmetry that involves phonons near the *K* zone boundary.[25] A stretching mode appears in aromatic rings of G-band (∼1540 cm^{-1}) pertaining to the Brillouin/optical zone center vibrations of E_{2g} mode in sp^2 bond present at the grain boundaries.[26−30]

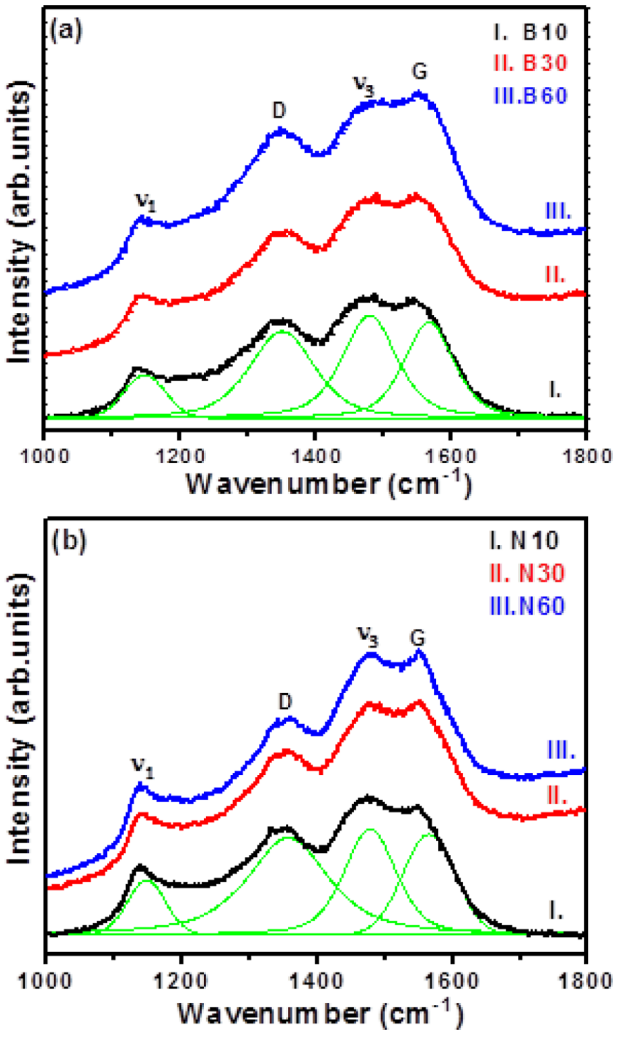

Figure 4. (a, b) Raman spectra of UNCD films grown for different growth times using (a) applied bias voltage (−200 V) and (b) no bias.

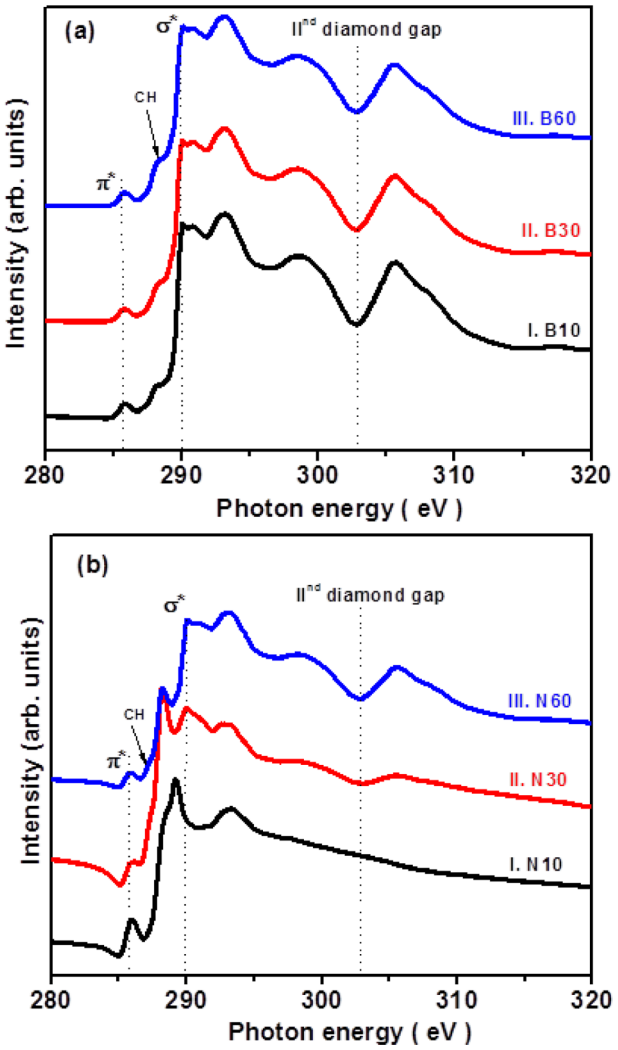

Figure 5. NEXAFS spectra of UNCD films deposited for different growth times in (a) bias (−200 V) and (b) no bias.

The broad peaks are suggestive of the small size of grains in the films. A small kink is observed at ∼1475 cm^{-1}, which is designated as ν_3 and is also assigned to contributions from *t*-PA segments present at the grain boundaries.[23,24] It should be noted that the Raman resonance peaks are several times more sensitive to the sp^2-bonded carbon that to the sp^3-bonded ones and are not able to provide unambiguous information about the sp^2/sp^3 ratio of the UNCD films. To more explicitly differentiate various types of carbon bonding configuration in the films, we used the NEXAFS spectroscopy.

Panels a and b in Figure 5 show, respectively, the NEXAFS spectra of the UNCD films deposited in CH_4/Ar plasma with and without bias at different growth times. The films grown using bias (curves I−III, Figure 5a) are clearly ascertaining that the major configuration of carbon is the sp^3 diamond phase with a smaller amount of sp^2 phase distributed in the films.[31] The sharp peak at ∼289.5 eV corresponds to the diamond electron core excitation of C−C (1s)-σ^* of the diamond phase, and the weak dip observed at 302.0 eV corresponds to the second absorption band gap of diamond.[32−34] The small peak at ∼285,5 eV is assigned to the C 1s-π^* transition corresponding to the sp^2 phase.[35,36] Moreover, a weak bump at 286.7 eV observed between π^* and σ^* bonds is attributed to the C−H bond,[37] which originates from the absorption of hydrocarbon at grain boundaries during the film deposition process.[38] In contrast, the films grown without bias for the growth time of 10 min (curve I, Figure 5b) show a large peak at ∼287.5 eV along with π^* band near 285.5 eV, which indicates that the films were predominated with the sp^2 phase and the peaks corresponding to diamond phase is not observable. But for $UNCD_{N60}$ films shows the sharp peak at 289.5 eV and weak dip at 302.2 eV, besides the π^* band near 285.5 eV and CH band near 287.5 eV, confirming the content of the diamond phase (curve III, Figure 5b). The $UNCD_{N30}$ films are also predominated with sp^2-bonded carbon (π^*-band at 285.5 eV), but with some proportion of sp^3-bonded carbon (σ^*-band at 289.5 eV), indicating that the coexistence of diamond grains with the amorphous phase. These results indicate that for the films grown without bias in CH_4/Ar plasma, the a-C phase formed first. It needs more than 30 min to nucleate the diamond grains. In contrast, for the films grown with bias, the diamond grains were nucleated instantaneously right after the application of bias.

The better PI characteristics of $UNCD_{B10}$ films are intimately correlated with their superior EFE properties. But the question arising now is what is/are the genuine factor(s) enhancing the EFE properties of $UNCD_{B10}$ films? To understand the mechanism that alters the EFE behavior of the films deposited

dx.doi.org/10.1021/am502231d | ACS Appl. Mater. Interfaces 2014, 6, 10566−10575

in CH_4/Ar plasma using bias and no bias at different growth times, TEM microstructure of the films were investigated to examine the changes of the hybridized carbon phase in the films. The bright field (BF) TEM image of $UNCD_{B10}$ (Figure 6a) shows that the films consist of diamond grains about 20−30 nm in size. Detailed examination of the selected area electron diffraction pattern (SAED) (inset, Figure 6a) reveals the commonly observed (111), (220) and (311) diffraction rings corresponding to the structure of diamond phase. The SAED rings are spotty rather than forming a smooth ring that is due to the relative large grains contained in these films. In the BF-TEM image of $UNCD_{B60}$ (Figure 6b), the grains are around a few tens of nanometers in size, which are about twice as large as the grains in $UNCD_{B10}$ (c.f. Figure 6a). The diamond grains are also randomly oriented, resulting in spotty ring patterns in the SAED image (inset, Figure 6b).

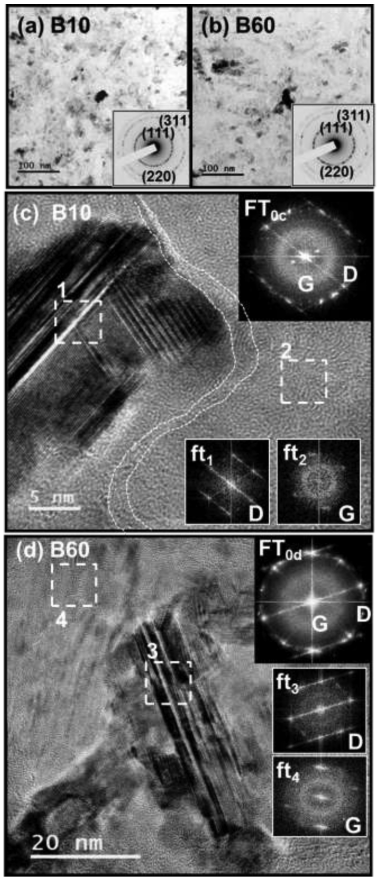

Figure 6. Bright-field TEM images of (a) $UNCD_{B10}$ and (b) $UNCD_{B60}$, films with the insets showing the corresponding SAED patterns. (c, d) The TEM structure images of the typical areas in (c) $UNCD_{B10}$ and (d) $UNCD_{B60}$ films. The insets FT_{0c} and FT_{0d} show the Fourier-transformed image corresponding to the whole structure image in "c" and "d", respectively, whereas the ft_1 to ft_4 images show the FT image corresponding to areas 1 to 4, respectively.

The detailed microstructure of the diamond grains in $UNCD_{B10}$ and $UNCD_{B60}$ films was examined using high-resolution TEM and was shown as TEM structure image in panels c and d in Figure 6, respectively. Figure 6c indicates that the large diamond grains in these films consist of parallel fringes. Some of the parallel fringes are irregular in spacing, which corresponds to stacking faults,[39,40] which is illustrated in area 1 and Fourier-transformed image ft_1, and some are regular in spacing, corresponding to hexagonal diamond.[39,40] The presence of planar defects in the diamond grains implies that the coalescence process has occurred during the growth of large diamond grains in the films. Moreover, there exists a diffuse ring in the center of Fourier-transformed (FT) image corresponding to the whole structure image in Figure 6c (FT_{0c}) that inferred the presence of some proportion of sp^2-bonded phase in this region. A typical region containing sp^2-bonded phase is illustrated by area 2 along with the ft_2 image. Notably, although the structure image in Figure 6c seems to contain large proportion of nondiamond phase as it shows no lattice fringes, the more detailed analyses using EELS, which will be shown shortly, reveals that this fringeless regions are actually of diamond structure, which are oriented away from a zone axis weakly and diffract the electrons, rendering the structure image of graphitic phase observable. Similarly, TEM structure image in Figure 6d shows that the $UNCD_{B60}$ films also contain diamond grains with large proportion of planar defects, as they contains parallel fringes in the structure image. The diamond grains in $UNCD_{B60}$ films are larger, ~20 × 50 nm. Again, the regions nearby the diamond grains are featureless. However, EELS analysis (will be shown shortly) indicates that this region also are mostly sp^3-bonded diamond grains, which are oriented in a weakly diffraction direction. The ft_4 image shows that this region contains sp^2-bonded phase, which is implied by the central diffuse diffraction rings in ft_4 images.

In contrast, the BF-TEM image of $UNCD_{N10}$ (Figure 7a) along with the SAED pattern (inset, Figure 7a) shows that the films consist of large diamond grains as like the $UNCD_{10B}$ films but with slightly smaller size. In contrast, in the BF image of $UNCD_{N60}$ films (Figure 7b), the grains are observed to grow to a size larger than hundreds of nanometer and are randomly oriented, resulting in spotty diffraction patterns. Images c and d in Figure 7 show the TEM structure images for $UNCD_{N10}$ and $UNCD_{N60}$ films, respectively, revealing that these films also contains diamond grains with large proportion of planar defects. The grain size of $UNCD_{N60}$ films are enormously larger than that of $UNCD_{N10}$ films, indicating the occurrence of marked grain growth against the growth time. Again, although the TEM structure images c and d in in Figure 7 shows the presence of featureless phase nearby the diamond grains, the EELS analyses (will be illustrated shortly) indicated that this featureless region is actually of sp^3-bonded carbons, the diamond grains, oriented in a nondiffracting direction. Moreover, the diffuse diffraction signal present in the center of FT_{0c} and FT_{0d} images in these figure indicated that the featureless phase contain large proportion of sp^2-bonded phase. It should be noted that the geometry of central diffuse diffraction rings in FT_{0c} image for $UNCD_{B10}$ films (Figure 6c) and FT_{0d} image for $UNCD_{B60}$ films (Figure 6c) are different from those in FT_{0c} image for $UNCD_{N10}$ films (Figure 7c) and FT_{0d} image for $UNCD_{N60}$ films (Figure 7c). The diffuse rings for $UNCD_{B10}$ and $UNCD_{B60}$ films are of "donut" geometry, inferring that the sp^2-bonded carbons in these materials are nanographitic phase, whereas those for $UNCD_{N10}$ and $UNCD_{N60}$ films are of "full-moon" geometry, inferring that the sp^2-bonded carbons in these materials are a-C phase. Intriguingly, the nanographitic phase in UNCDB10 films is so abundant that they formed a interconnected filament, designated by a pair of dotted curves in Figure 6c. No such interconnected filament was observable for other UNCD films.

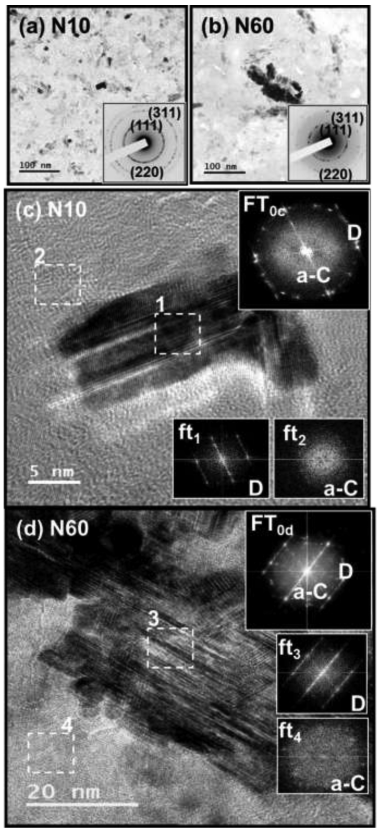

Figure 7. Bright-field TEM images of (a) $UNCD_{N10}$ and (b) $UNCD_{N60}$, films with the insets showing the corresponding SAED patterns. (c, d) The TEM structure images of the typical areas in (c) $UNCD_{N10}$ and (d) $UNCD_{N60}$ films. The insets FT_{0c} and FT_{0d} show the Fourier-transformed image corresponding to the whole structure image in "c" and "d", respectively, whereas the ft_1 to ft_4 images show the FT image corresponding to areas 1 to 4, respectively.

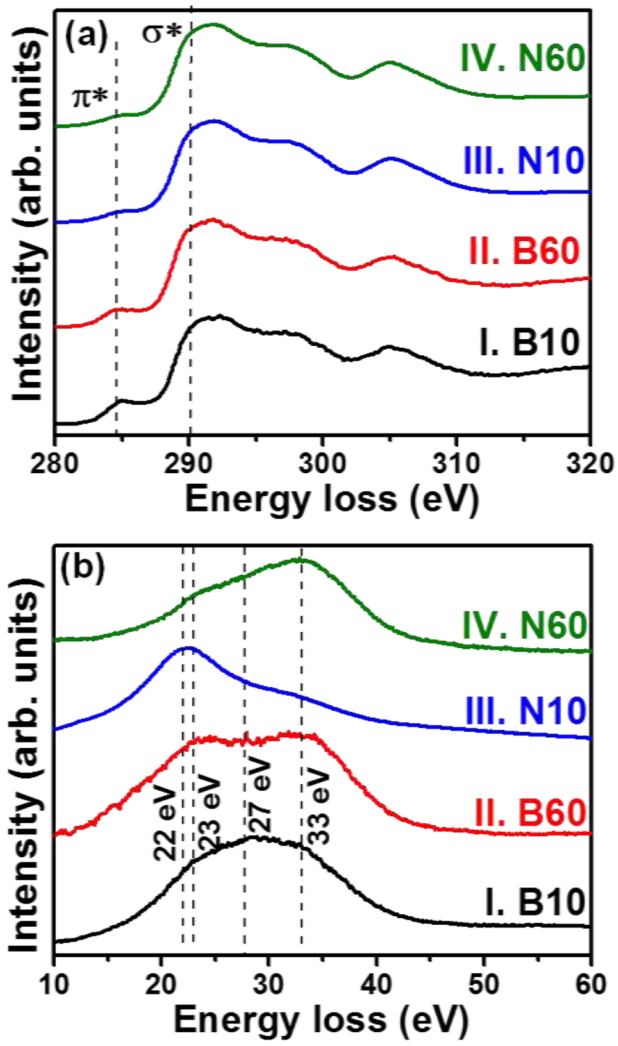

Figure 8. Selected area EELS spectra of the UNCD films: (a) core-loss EELS spectra and (b) plasmon-loss EELS spectra for (I) $UNCD_{B10}$, (II) $UNCD_{B60}$, (III) $UNCD_{N10}$, and (IV) $UNCD_{N60}$ films.

The different behavior in modifying the microstructure of the UNCD films due to bias is interesting, but such information is not able to account for the different degree of improvement on the EFE properties of the $UNCD_{B10}$ films. To understand the genuine mechanism on the enhancement of those properties, we examined the bonding structure of the UNCD films using EELS. Figure 8 shows the selected area EELS spectra corresponding to each TEM BF-micrograph in Figures 6 and 7, revealing that, there are significant changes in bonding structures due to the application of bias voltage in MPE-CVD process. The carbon edge core-loss EELS spectra corresponding to these UNCD films (Figure 8a) indicate that, for all of the UNCD films, there present an abrupt rise near 289.5 eV (σ*-band) and a large dip in the vicinity of 302 eV, implying the diamond nature of these materials.[41,42] Moreover, there is a prominent π*-band at 284.5 eV in core-loss EELS spectra, especially for $UNCD_{B10}$ (curve I) and $UNCD_{B60}$ films (curve II), indicating that some proportion of sp^2-bonded carbon was induced.

However, it is still necessary to differentiate the nature of the sp^2-bonded carbon to understand the genuine mechanism for enhancing the EFE properties for the UNCD films grown using bias compared with those grown without bias. It should be pointed out that the plasmon-loss EELS spectra is the most effective measurement for distinguishing the crystalline sp^2-bonded carbons (the graphite) from the noncrystalline sp^2-bonded ones (amorphous carbons), as the plasmon-loss EELS spectra for the graphitic phase shows a prominent peak at s_3 (27 eV) and those for the a-C phase shows a peak at s_1 (22 eV).[41,42] In contrast, the diamond shows a peak consequent to the bulk plasmon at s_4 (33 eV) with a shoulder corresponding to the surface plasmon at s_2 (23 eV) with the I_{s2}/I_{s4} ratio is about $1:\sqrt{2}$.[41,42] Figure 8b shows the plasmon-loss EELS spectra of the same regions, from which the core-loss EELS spectra were acquired. It is observed that $UNCD_{B10}$ films (curve I, Figure 8b) are dominated by larger s_3-band (~27 eV), representing the graphitic phase, with the s_2 and s_4-bands (representing diamond)[39] of much smaller intensity, i.e., this region consists of large proportion of graphitic phases besides diamond. The interconnected filaments are conducting paths for transporting electrons and are presumed to be the genuine factor that enhanced the EFE properties of the $UNCD_{B10}$ films. In contrast, the plasmon-loss EELS spectrum of $UNCD_{B60}$ films (curve II, Figure 8b) are dominated with s_2 and s_4 peaks, with much smaller proportion of s_3-band, indicating that the $UNCD_{B60}$ films are predominated with diamond. The proportion of graphitic phase decreased markedly as the grain grew larger in size.

Quite the opposite, the plasmon-loss spectrum for $UNCD_{N10}$ films (curve III, Figure 8b) is subjugated by s_1-band (22 eV), in which s_2- and s_4-bands still present but with much smaller in spectral weight. This result indicates that the $UNCD_{N10}$ films grown without bias are predominated with a-C phases. Only small number of diamond grains was nucleated in the films, i.e., the proportion of diamond grains in these films is much less. In contrast, the plasmon-loss EELS spectrum for $UNCD_{N60}$ films (curve IV, Figure 8b) is predominated with s_2- and s_4-bands corresponding to diamond phase, with a very small proportion of s_1-band corresponding to a-C phase that is similar to the plasmon-loss EELS spectrum for $UNCD_{B60}$ films.

These observations indicate that the a-C phase was formed preferentially when the UCND films were grown without bias voltage such that the $UNCD_{N10}$ films are predominated with a-C phase that is schematically illustrated as steps (i) and (ii) in Figure 9a. The proportion of diamond grains in the films grown without bias increased with the growth time along with the increase in grain size and eventually occupied the whole region of the films for $UNCD_{N60}$ films, in which The a-C phase was effectively eliminated that is schematically illustrated a step (iii) in Figure 9a. In contrast, for the films grown in bias, the diamond grains were nucleated instantaneously for $UNCD_{B10}$ films, along with the formation of some proportion of graphitic phases in the grain boundary regions of the films, forming the interconnected graphitic filaments that are schematically illustrated as steps (i) and (ii) in Figure 9b. The size of diamond grains increases with growth time. The graphitic phase is still present for the $UNCD_{B60}$ films but with much smaller proportion (schematically illustrated as step in Figure 9b). Notably, the sp^2-bonded carbon in $UNCD_{B10}$ and $UNCD_{B60}$ films is crystalline, i.e., the nanographitic phase rather a-C. The grains also grew in size with the growth time, but the size of the grains is limited to around 2−3 times as large as the as-nucleated diamond grains. The diamond grains in BEG grown UNCD films remained at small size due to the enhanced renucleation rate for the diamond clusters under the application of negative bias voltage to the substrates. Such a phenomenon is in accord with the literature reports.[17−19] Interestingly, there is always presence of some graphitic phase, even for $UNCD_{B60}$ films, which were grown for 60 min.

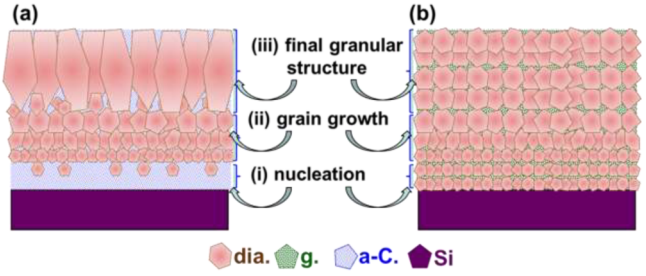

Figure 9. Schematics showing the evolution process for the granular structure for the UNCD films grown (a) without and (b) with the bias: (i) the diamond grains were scarcely nucleated among the a-C phase without the bias in "a" but were nucleated instantaneously with bias in "b"; (ii) the grain size increased with growth time; and (iii) big diamond grains were resulted with very few grain boundary phase for the films grown without bias in "a", whereas the grains only grew moderately with the coexistence of some graphitic phase when grown with bias in "b".

Previous reports revealed that the graphitic phases are more conducting than that of the a-C phases,[43] such that the formation of sp^2-bonded graphitic phases at the grain boundaries creates conduction channels for the electrons to transport from the bottom of the films to the top side and emit to vacuum very easily. In this work, the application of bias induces nanographite phases in the grain boundaries of the UNCD films such that the electrons can be transported easily along the graphite phases to the emitting surface and were then emitted to vacuum without any difficulty as the diamond surfaces are NEA in nature.[44,45] Especially, $UNCD_{B10}$ films show the formation of interconnected nanographitic filaments and thus possess the superior EFE properties to the $UNCD_{B60}$ films compared to that of the other UNCD films. Moreover, the smaller $(E_0)_{EFE}$ of $UNCD_{B10}$ films can emit the electrons at lower voltages, which can participate in ionizing the Ar gas molecules of PI studies. As a result, there will be a significant enhancement in J_{PI}, which follows the same trend as the EFE behavior. Restated, the induction of graphitic phases in the grain boundaries because of bias voltage is presumed to be the genuine factor for the superior EFE properties of $UNCD_{B10}$ films.

CONCLUSIONS

UNCD films were grown for different growth times in CH_4/Ar plasma using BEN-BEG process in MPECVD system. The changes in the sp^2 and sp^3 carbon phases in the films due to the change in growth time and the application of bias voltage are studied by analysis in detail. The BEN-BEG UNCD films possess higher growth rate than that of the films grown without bias. Moreover, while applying bias, the diamond grains are formed at the beginning of growth, but the films grown without bias needs more than 30 min for the formation of diamond grains. Transmission electron microscopy investigation reveals that the application of bias voltage stimulate the formation of nanographite phases in the grain boundaries of the UNCD films such that the electrons can be transported easily along the graphite phases to the emitting surface and shows better EFE properties. Interestingly, the UNCD films grown for 10 min under bias offer the lowest turn-on field of 4.2 V/μm and the highest EFE current density of 2.6 mA/cm^2 at the applied field of 7.85 V/μm, because the films possess ultrananno diamond grains with more graphitic grain boundary phases. But the films grown for 60 min using bias possess large clustered grains that hinder the transport of electrons resulting inferior EFE properties. On the other hand, the films grown without bias have mostly a-C phases and lesser amount of diamond grains, showing poorer EFE properties than the films grown using bias. The PI properties were closely correlated with the EFE properties of the UNCD films, which are found to be responsive to change in the microstructure of UNCD films. Investigations based on the PI properties of UNCD films support their potential utilize in display and field-emission applications.

ASSOCIATED CONTENT

Supporting Information

Details on the optical emission spectroscopy, secondary electron emission coefficient measurements, and TEM microstructures, with corresponding figures. This material is available free of charge via the Internet at http://pubs.acs.org.

AUTHOR INFORMATION

Corresponding Author

*E-mail: inanlin@mail.tku.edu.tw.

Notes

The authors declare no competing financial interest.

■ ACKNOWLEDGMENTS

The authors are thankful for the financial support of National Science Council of Republic of China through the project NSC 102-2112-M-032-006.

■ REFERENCES

(1) Pradhan, D.; Lin, I. N. Grain Size Dependent Diamond-Nondiamond Composite Films: Characterization and Field Emission Properties. *ACS Appl. Mater. Interfaces* **2009**, *7*, 1444−1450.
(2) Liu, H.; Dandy, D. S. Studies on Nucleation Process in Diamond CVD: An Overview of Recent Developments. *Diamond Relat. Mater.* **1995**, *4*, 1173−1188.
(3) Angus, J. C.; Will, H. A.; Stanko, W. S. Growth of Diamond Seed Crystals by Vapor Deposition. *J. Appl. Phys.* **1968**, *39*, 2915−2922.
(4) Spitsyn, B. V.; Bouilov, L. L.; Derjaguin, B. V. Vapor Growth of Diamond on Diamond and Other Surfaces. *J. Cryst. Growth.* **1981**, *52*, 219−226.
(5) Chen, Y. C.; Zhong, X. Y.; Konicek, A. R.; Grierson, D. S.; Tai, N. H.; Lin, I. N. Synthesis and Characterization of Smooth Ultrananocrystalline Diamond Films via Low Pressure Bias-enhanced Nucleation and Growth *J. Appl. Phys.* **2008**, *92*, No. 133113.
(6) Geis, M. W.; Efremow, N. N.; Woodhouse, J. D.; Mcaleese, M. D.; Marchywka, M.; Socker, D. G.; Hochedez, J. F. Diamond Cold Cathode. *IEEE Electron Device Lett.* **1991**, *12*, 456−459.
(7) Kang, W. P.; Davidson, J. L.; Wisitsoraat, A.; Kerns, D. V.; Kerns, S. Recent Development of Diamond Microtip Field Emitter Cathodes and Devices. *J. Vac. Sci. Technol.* **2001**, *19*, 936−941.
(8) Bachmann, P. K.; van Elsbergen, V.; Wiechert, D. U.; Zhong, G.; Robertson, J. CVD Diamond: A Novel High γ-coating for Plasma Display Panels? *Diamond Relat. Mater.* **2001**, *10*, 809−817.
(9) Chakrabarti, K.; Chakrabarrti, R.; Chattopadhyay, K. K.; Chaudhrui, S.; Pal, A. K. Nano-Diamond Films Produced from CVD of Camphor. *Diamond Relat. Mater.* **1998**, *7*, 845−852.
(10) Sowers, A. T.; Ward, B. L.; English, S. L.; Nemanich, R. J. Field Emission Properties of Nitrogen-Doped Diamond Film. *J. Appl. Phys.* **1999**, *86*, 3973−3982.
(11) Farrer, R. G.; Vermeulen, L. A. Photoconductivity in Irradiated Diamond. *J. Phys. C* **1972**, *5*, 2762−2768.
(12) Joseph, P. T.; Tai, N. H.; Niu, H.; Palnitkar, U. A.; Pong, W. F.; Cheng, H. F.; Lin, I. N. Structural Modification and Enhanced Field Emission on Ultrananocrystalline Diamond Films by Nitrogen Ion Implantation. *Diamond Relat. Mater.* **2008**, *17*, 1812−1816.
(13) Corrigan, T. D.; Krauss, A. R.; Gruen, D. M.; Auciello, O.; Chang, R. P. H. Low Temperature Growth of Nanocrystalline Diamond Films on Glass Substrates for Field Emission Applications. *Mater. Res. Soc. Symp. Proc.* **2000**, *593*, 233−236.
(14) Tsugawa, K.; Ishihara, M.; Kim, J.; Hasegawa, M.; Koga, Y. Large Area and Low Temperature Nanodiamond Coating by Microplasma Chemical Vapor Deposition. *New Diamond Front. Carbon Technol.* **2006**, *16* (6), 337−346.
(15) Zhou, D.; Krauss, A. R.; Qin, L. C.; McCauley, T. G.; Gruen, D. M.; Corrigan, T. D.; Chang, R. P. H.; Gnaser, H. Synthesis and Electron Field Emission of Nanocrystalline Diamond Thin Films Grown from N_2/CH_4 Microwave Plasmas. *J. Appl. Phys.* **1997**, *82*, 4546−4550.
(16) Krauss, A. R.; Gruen, D. M.; Zhou, D.; McCauley, T. G.; Qin, L. C.; Corrigan, T. D.; Auciello, O.; Chang, R. P. H. Morphology and Electron Emission Properties of Nanocrystalline CVD Diamond Thin Films. *Mater. Res. Soc. Symp. Proc.* **1998**, *495*, 299−310.
(17) Chu, Y. C.; Tu, C. H.; Liu, C.; Tzeng, Y.; Auciello. O. Ultrananocrystalline Diamond Nano-Pillars Synthesized by Microwave Plasma Bias-Enhanced Nucleation and Bias-Enhanced Growth in Hydrogen-Diluted Methane *J. Appl. Phys.* **2012**, *112*, No. 124307.
(18) Zhong, X. Y.; Chen, Y. C.; Tai, N. H.; Lin, I. N.; Hiller, J. M.; Auciello, O. Effect of Pretreatment Bias on the Nucleation and Growth Mechanisms of Ultrananocrystalline Diamond Films via Bias-Enhanced Nucleation and Growth: An Approach to Interfacial Chemistry Analysis via Chemical Bonding Mapping *J. Appl. Phys.* **2009**, *105*, No. 034311.
(19) Teng, K. Y.; Chen, H. C.; Tzeng, G. C.; Tang, C. Y.; Cheng, H. F.; Lin, I. N. Bias-Enhanced Nucleation and Growth Processes for Improving the Electron Field Emission Properties of Diamond Films *J. Appl. Phys.* **2012**, *111*, No. 053701.
(20) Thomas, J. P.; Chen, H. C.; Tseng, S. H.; Wu, H. C.; Lee, C. Y.; Cheng, H. F.; Tai, N. H.; Lin, I. N. Preferentially Grown Ultranano c-Diamond and n-Diamond Grains on Silicon Nanoneedles from Energetic Species with Enhanced Field-Emission Properties. *ACS Appl. Mater. Interface* **2012**, *4*, 5103−5108.
(21) Fowler, R. H.; Nordheim, L. Electron Emission in Intense Electric Fields. *Proc. R. Soc. London, Ser. A* **1928**, *119*, 173−181.
(22) Bogaerts, M.; Gijbels, R.; Goedheer, W. Modeling of Ionization of Argon in an Analytical Capacitively Coupled Radio-frequency Glow Discharge. *J. Appl. Phys.* **1999**, *86*, 2990−3001.
(23) Pfeiffer, R.; Kuzmany, H.; Knoll, P.; Bokova, S.; Salk, N.; Gunther, B. Evidence for *Trans*-Polyacetylene in Nano-Crystalline Diamond Films. *Diamond Relat. Mater.* **2003**, *12*, 268−271.
(24) Piazza, F.; Golanski, A.; Schulze, S.; Relihan, G. Trans-polyacetylene Chains in Hydrogenated Amorphous Carbon Films free of Nanocrystalline Diamond *Appl. Phys. Lett.* **2003**, *82*, No. 358360.
(25) Wu, Z. S.; Pei, S.; Ren, W.; Tang, D.; Gao, L.; Liu, B.; Li, F.; Cheng, H. M. Field Emission of Single-Layer Graphene Films Prepared by Electrophoretic Deposition. *Adv. Mater.* **2009**, *21*, 1756−1760.
(26) Birrell, J.; Gerbi, J. E.; Auciello, O.; Gibson, J. M.; Johnson, J.; Carlisle, J. A. Interpretation of the Raman spectra of ultrananocrystalline diamond. *Diamond Relat. Mater.* **2005**, *14*, 86−92.
(27) Xiao, X.; Birrell, J.; Gerbi, J. E.; Auciello, O.; Carlisle, J. A. Low temperature growth of ultrananocrystalline diamond. *J. Appl. Phys.* **2004**, *96*, 2232−2239.
(28) Chen, Q.; Gruen, D. M.; Krauss, A. R.; Corrigan, T. D.; Witek, M.; Swain, G. M. J. The Structure and Electrochemical Behavior of Nitrogen- Containing Nanocrystalline Diamond Films Deposited from $CH_4/N_2/Ar$ Mixtures. *Electrochem. Soc.* **2001**, *148*, E44−E41.
(29) Kuzmany, H.; Pfeiffer, R.; Salk, N.; Gunther, B. The Mystery of the 1140 cm^{-1} Raman line in Nanocrystaline Diamond Films. *Carbon* **2004**, *42*, 911−917.
(30) Ferrari, A. C.; Robertson, J. Origin of the 1150 cm^{-1} Raman Mode in Nanocrystalline Diamond *Phys. Rev. B*, **2001**, *63*, No. 121405.
(31) Sankaran, K. J.; Kurian, J.; Chen, H. C.; Dong, C. L.; Lee, C. Y.; Tai, N. H.; Lin, I. N. Origin of a Needle-like Granular Structure for Ultrananocrystalline Diamond Films Grown in a N_2/CH_4 Plasma *J. Phys. D: Appl. Phys.* **2012**, *45*, No. 365303.
(32) Birrell, J.; Gerbi, J. E.; Auciello, O.; Gibson, J. M.; Gruen, D. M.; Carlisle, J. A. Bonding Structure in Nitrogen Doped Ultrananocrystalline Diamond. *J. Appl. Phys.* **2003**, *93*, 5606−5612.
(33) Joseph, P. T.; Tai, N. H.; Chen, C. H.; Niu, H.; Pong W. F.; Lin, I. N. On the Mechanism of Enhancement on Electron Field Emission Properties for Ultrananocrystalline Diamond Films due to Ion Implantation *J. Appl. Phys.* **2009**, *42*, No. 105403.
(34) Nithianandam, J.; Rife, J. C.; Windischmann, H. Carbon *K* edge Spectroscopy of Internal Interface and Defect States of Chemical Vapor Deposited Diamond Films. *Appl. Phys. Lett.* **1992**, *60*, 135−137.
(35) Gutierrez, A.; Lopez, M. F.; Garcia, I.; Vazquez, A. X-ray Absorption and Auger Electron Spectroscopy Studies of the Quality of Diamond Thin Films grown by the Oxy-acetylene Flame Method. *J. Vac. Sci. Technol.* **1997**, *15*, 294−297.
(36) Chen, S. S.; Chen, H. C.; Wang, W. C.; Lee, C. Y.; Lin, I. N.; Guo J.; Chang, C. L. Effects of High Energy Au-ion Irradiation on the Microstructure of Diamond Films *J. Appl. Phys.* **2013**, *113*, No. 113704.
(37) Ponsonnet, L.; Donnet, C.; Varlot, K.; Martin, J. M.; Grill, A.; Patel, V. EELS Analysis of Hydrogenated Diamond-like Carbon Films. *Thin Solid Films* **1998**, *319*, 97−100.

(38) Lin, I. N.; Chen, H. C.; Wang, C. S.; Lee, Y. R.; Lee, C. Y. Nanocrystalline Diamond Microstructures from $Ar/H_2/CH_4$-plasma Chemical Vapour Deposition. *CrystEngComm* **2011**, *13*, 6082−6089.
(39) Gruen, D. M.; Liu, S.; Krauss, A. R.; Luo, J.; Pan, X. Fullerenes as Precursors for Diamond Film Growth Without Hydrogen or Oxygen Additions. *Appl. Phys. Lett.* **1994**, *64*, 1502−1504.
(40) Kovarik, P.; Bourdon, E. B. D.; Prince, R. H. Electron Energy Loss Characterization of Laser-deposited *a*-C, *a*-C:H and Diamond Films. *Phys. Rev. B* **1993**, *48*, 12123−12129.
(41) Prawer, S.; Peng, J. L.; Orwa, J. O.; McCallum, J. C.; Jamieson, D. N.; Bursill, L. A. Size Dependence of Structural Stability in Nanocrystalline Diamond *Phys. Rev. B* **2000**, *62*, No. R16360.
(42) Arenal, R.; Bruno, P.; Miller, D. J.; Bleuel, M.; Lal, J.; Gruen, D. Diamond nanowires and the insulator-metal transition in ultra-nanocrystalline diamond films *Phys. Rev. B* **2007**, *75*, No. 195431.
(43) Cui, J. B.; Stammler, M.; Ristein, J.; Ley, L. Role of Hydrogen on Field Emission from Chemical Vapor Deposited Diamond and Nanocrystalline Diamond Powder. *J. Appl. Phys.* **2000**, *88*, 3667−3673.
(44) Yamaguchi, H.; Masuzawa, T.; Nozue, S.; Kudo, Y.; Saito, I.; Koe, J.; Kudo, M.; Yamada, T.; Takakuwa, Y.; Okano, K. Electron Emission from Conduction Band of Diamond with Negative Electron Affinity *Phys. Rev. B* **2009**, *80*, No. 165321.
(45) Geis, M. W.; Deneault, S.; Krohn, K. E.; Marchant, M.; Lyszczarz, T. M.; Cooke, D. L. Field Emission at $10V\ Cm^{-1}$ with Surface Emission Cathodes on Negative-Electron-Affinity Insulators. *Appl. Phys. Lett.* **2005**, *87*, No. 192115.